

# Critical soil moisture detection and water-energy limit shift attribution using satellite-based water and carbon fluxes over China

Yi Liu<sup>1</sup>, Jingfeng Xiao<sup>2</sup>, Xing Li<sup>3</sup>, Yue Li<sup>4</sup>

<sup>1</sup>School of Civil Engineering and Architecture, Guangxi University, Nanning 530004, China

5 <sup>2</sup>Earth Systems Research Center, Institute for the Study of Earth, Oceans, and Space, University of New Hampshire, Durham, NH 03824, USA

<sup>3</sup>School of Geography and Planning, Sun Yat-Sen University, Guangzhou 510275, China

<sup>4</sup>Department of Earth Sciences, Indiana University-Purdue University Indianapolis (IUPUI), Indianapolis, IN 46202, USA

*Correspondence to:* Yi Liu (liuyi.15b@igsnr.ac.cn)

10 **Abstract.** Critical soil moisture (CSM), a tipping point of soil moisture (SM) at which surface fluxes shift from the energy to the water-limited regime, is essential for the vegetation state and the corresponding land-atmosphere coupling. However, detecting CSM and attributing water-energy limit shifts to climate and ecosystem variables are challenging as in-situ observations of water, carbon fluxes, and SM are sparse. In this study, CSM was assessed over China using two satellite-based methods: the difference between the correlation between SM and evapotranspiration (ET) and the correlation between  
15 vapor pressure deficit (VPD) and ET; the covariance between VPD and gross primary production (GPP). ET and GPP products were based on the Penman-Monteith-Leuning (PML) ET and GPP, Global LAnd Surface Satellite (GLASS) ET and GPP, Collocation-Analyzed Multi-source Ensembled Land Evapotranspiration (CAMELE) ET, Surface Energy Balance Algorithm for Land (SEBAL) ET, Two-Leaf light use efficiency model based (TL) GPP, and SIF-based (GOSIF) GPP. At flux sites, ET and GPP products were evaluated by eddy covariance-based measurements; CSM values using two satellite-  
20 based methods were assessed by CSM using the soil moisture-evaporative fraction method. Their consistency at site scales demonstrated reliable results and applicability to regional scales. Through intercomparison, the spatial pattern of CSM from multi-source ET and GPP datasets was consistent and robust in eastern and southern China. Generally, CSM decreased from south to north. Pearl River Basin and Southeastern River Basin displayed a relatively high CSM for clay-rich soils (e.g., 0.39 m<sup>3</sup>/m<sup>3</sup> using PML ET and 10 cm depth SM) and forests (e.g., 0.35 m<sup>3</sup>/m<sup>3</sup> using PML ET and 10 cm depth SM). At four soil  
25 layers, CSM for grassland and clay was higher than average SM, making them in water-limited regimes. Thus, western grassland was more susceptible to water stress with increased water demand. These findings highlight the variability in CSM and primary determinants of water-energy limit shifts, offering valuable insights into the potential water limitation on ecosystems under comparable SM circumstances.

## 1 Introduction

30 Critical soil moisture (CSM) serves as an indicator of shifts in the relationship between water and energy availability (Schwingshackl et al., 2017; Denissen et al., 2020) and is essential in shaping regional climates. Plants adjust their stomatal resistance in response to changes in soil moisture (SM) and vapor pressure deficit (VPD) (Grossiord et al., 2020; Li, F. et al., 2023). Above CSM, there is no alteration in water stress with SM increases (Rodriguez-Iturbe, 2000; Seneviratne et al., 2010; Akbar et al., 2018); plants are primarily controlled by VPD. Warm and dry air above the canopy (Grossiord et al., 2020; Li, X. et al., 2023) leads to a decrease in both the transpiration process as the largest part of evapotranspiration (ET) (Good et al., 2015) and gross primary production (GPP) coupled with the ET process via plant leaf stomata (Gentine et al., 2019; Liu et al., 2020). A decrease in ET, in turn, results in elevated surface temperature and VPD (Gentine et al., 2019) and leads to increased atmospheric aridity on a large spatial scale, thereby intensifying SM depletion. Below CSM, surface fluxes are primarily influenced by SM availabilities in conditions of restricted water supply. During this period, a decrease in SM results in a reduction in latent heat flux (LE) and an increase in sensible heat flux (H) (Rodriguez-Iturbe, 2000); SM and leaf conductance follow a positive linear relationship (Laio et al., 2001; Porporato et al., 2002). Previous studies have examined land-atmosphere feedback using different metrics and both observation and simulation data (Seneviratne et al., 2006; Koster et al., 2009; Teuling et al., 2009). They found that water and energy limit shifts may be further strengthened by the interaction between the land and atmosphere, particularly when positive feedback mechanisms known as the "dry gets dryer" effect (Seneviratne et al., 2010; Gentine et al., 2019). Over extended temporal periods, this phenomenon may lead to the persistence of arid and high-temperature conditions (Zhang et al., 2020). Consequently, it is necessary to quantify the CSM characteristics and the influencing environmental factors of water and energy limit shifts.

Traditionally, under the framework based on the ratio of LE to the total of LE and H (Haghighi et al., 2018; Fu et al., 2022a), sparse eddy covariance observations (Feldman et al., 2019; Fu et al., 2022b) pose challenges in adequately capturing comprehensive regional or continental-scale CSM and its variations (Dong et al., 2023; Hsu and Dirmeyer, 2023a). In recent years, the feasibility of conducting large-scale analysis has been enhanced by the growing accessibility of multi-source remotely sensed datasets (Liu et al., 2012). Globally, some studies used the ratio of LE to net radiation (Seneviratne et al., 2010; Schwingshackl et al., 2017), surface temperature diurnal amplitude (Feldman et al., 2019; Fu et al., 2024), and LE (Hsu and Dirmeyer, 2023b; Duan et al., 2023). In addition, advancement of global remote sensing products technology has facilitated the generation of reliable GPP products (Yuan et al., 2014; Li and Xiao, 2019; Zhang et al., 2019; Bi et al., 2022; He et al., 2022; Li, F. et al., 2023) and ET products (Yao et al., 2013; Yao et al., 2014; Zhang et al., 2019; Cheng et al., 2021; He et al., 2022; Li, C. et al., 2022; Li, F. et al., 2023) for CSM detection. Denissen et al. (2020) proposed a new tipping-point metric, the difference between the correlation between SM and ET and the correlation between VPD and ET, to directly determine CSM at continental scales. Fu et al. (2022b) first demonstrated that the covariance between GPP and VPD indirectly quantifies CSM. The point at which covariance between GPP and VPD transitions from positive to negative during a period of soil drying is denoted as CSM. However, a source of considerable uncertainty when considering only a single

data source and estimation approach exists at a large spatial scale. There are significant differences among satellite-based ET and GPP datasets, and CSM varies with different methods, leading to uncertainty as to whether CSM of carbon flux is the same as that of water flux.

65 Chinese land surface frequently experiences water and energy limit shifts (Xiao, 2014; Zhu et al., 2023). Diagnosing large-scale CSM helps to understand water- and energy-limited regimes determined by distinct flora and soil types (Homaee et al., 2002; Hsu and Dirmeyer, 2023b). The association between water, energy, and flux helps to define water and energy limit shifts. As such, this study uses two innovative metrics and eight satellite-based products to diagnose CSM and water and energy limit shifts across China. The goal of this study is to (1) assess the consistency of different methods in calculating  
70 CSM at flux sites; (2) examine CSM variations across land cover types, soil textures, and water resource subregions; and (3) investigate dominant factors from hydrological, meteorological, and ecological variables that influence water and energy limit shifts.

## 2 Material and methods

### 2.1 Data

75 Eddy covariance flux datasets were compared with eight satellite-based ET and GPP in Section 3.1. Then, CSM derived from the relationship between SM and evaporative fraction (EF) was used to evaluate the performance of CSM derived from the covariance and correlation-difference methods in Section 3.2. Layer-wise SM and satellite-based ET and GPP were used for the large-scale detection of CSM. Land cover types, soil textures, and water resource subregions were used to examine CSM variations in Section 3.3. SM, ET, GPP, and meteorological data were used to investigate dominant factors influencing  
80 water and energy limit shifts in Section 3.4. All energy, vegetation, and water variables were resampled or combined to 0.1°-8 days resolution. The period, limited by the temporal availability of data sources, covered 2001–2018.

#### 2.1.1 Evapotranspiration and gross primary production

Figure 1 illustrates locations of 21 flux sites, and Table 1 shows the detailed information on flux sites. Eddy covariance-derived measurements were applied to evaluate the performance of satellite-based ET and GPP. Given the fact that  
85 Huazhaizi, Dashalong, Luodi, Arou, Guantao, Huailai, Miyun, and Daxing did not have GPP data, the REddyProc website (<https://www.bgc-jena.mpg.de/5622399/REddyProc/>) was used to calculate GPP. REddyProc imported half-hourly net ecosystem exchange, LE, H, and meteorological measurements to partition net ecosystem exchange into GPP and ecosystem respiration.

Table 2 contains a list of all spatial data sets used in this study. Eight satellite-based ET and GPP products are included.  
90 Penman-Monteith-Leuning (PML) integrates the stomatal conductance theory to relate ET and GPP processes (Zhang et al., 2019; He et al., 2022) and applies daily meteorological data, land surface temperature from ERA5, enhanced Whittaker-filtered MODIS LAI, albedo, and emissivity. The interdependency and mutual restrictions between GPP and ET

considerably improve the simulation accuracy. Global LAnd Surface Satellite (GLASS) ET integrates the MOD16, a revised remote sensing-based Penman-Monteith, the Priestley-Taylor Jet Propulsion Laboratory, a modified satellite-based Priestley-Taylor, and the Semi-Empirical Algorithm of the University of Maryland using the Bayesian model averaging approach (Yao et al., 2013; Yao et al., 2014); GLASS GPP algorithm incorporates effects of atmospheric carbon dioxide content, radiation components, and VPD based on the eddy covariance-light use efficiency model introduced by Yuan et al. (2007). It is founded on two underlying assumptions: the fraction of absorbed photosynthetically active radiation has a linear relationship with the normalized difference vegetation index; constant light use efficiency is governed by either air temperature or soil moisture, depending on which component imposes the greatest limitation.

In addition, Collocation-Analyzed Multi-source Ensembled Land Evapotranspiration (CAMELE) provides long-term (1981–2020) ET, employing ERA5, FLUXCOM, PML, GLDAS, and GLEAM (Li, C. et al., 2022), at  $0.1^\circ$ -8 days and  $0.25^\circ$ -daily resolutions. Surface Energy Balance Algorithm for Land (SEBAL) ET focuses on 1 km-daily resolution during 2001–2018. This product integrates GMAO's meteorological data and NASA's MOD43A1 daily surface albedo, MOD11A1 daily surface temperature, and MOD13 vegetation index (Cheng et al., 2021). Two-Leaf light use efficiency model-based (TL) GPP offers comprehensive worldwide GPP, shaded GPP, and sunlit GPP covering the period from 1992 to 2020. This model applies recent data inputs such as the GLOBMAP LAI, CRUJRA meteorological data, and ESA-CCI land cover information (Bi et al., 2022). Global, Orbiting carbon observatory-2 SIF-based (GOSIF) GPP spans from 2000 to 2020. A total of eight SIF-GPP relationships, including both universal and biome-specific formulations, are used to estimate GPP from SIF on a per-pixel basis and examined with and without intercept terms to account for the uncertainty in converting SIF into GPP estimates (Li and Xiao, 2019).

### **2.1.2 Layer-wise soil moisture and meteorological data**

Given the recent availability of state-of-the-art gridded SM in China released by Li, Q. et al. (2022), CSM can now be investigated in the context of the SM state. Gridded SM reaches 100 cm soil depth with 10 cm intervals at 1 km-daily resolution during 2000–2020. It is trained by predictors of ERA5-Land time series, leaf area index (LAI), land cover type, topography, and in-situ observed soil attributes at 1789 stations throughout China, using the robust random forest machine learning technique. Based on the findings of Li, Q. et al. (2022), the product demonstrates notable benefits over both ERA5-Land and SMAP-L4 datasets, especially in terms of a superior quality level compared to the SoMo.ml dataset at soil depths of 10, 20, 80, and 100 cm. Thus, this study utilized SM of these layers.

Yang et al. (2010) and He et al. (2020) put forth a comprehensive dataset for Chinese regional surface meteorological forcing. This dataset encompasses air temperature, air pressure, specific humidity, wind speed, downward shortwave radiation, downward longwave radiation, and precipitation. It is presented in the NetCDF format with a spatiotemporal resolution of  $0.1^\circ$ -3 hours during 1979–2018. The primary input includes Princeton University's Global Land Surface Model Data, GLDAS, GEWEX-SRB radiation, TRMM precipitation, and China Meteorological Administration observations. Data quality control techniques include the elimination of physically implausible values and statistical interpolation using ANU-

Spline. This dataset demonstrates precision levels that lie between those of site-based observation and satellite-based estimation, therefore exceeding the accuracy of current international reanalysis datasets. In this study, VPD was computed by specific humidity and air temperature; VPD, air temperature, precipitation, and downward shortwave radiation were employed in water-energy limit shift attribution.

### 130 **2.1.3 Land cover types, soil textures, and water resource subregions**

Land cover types, soil textures, and water resource subregions influence CSM. Land cover types (2020) are created by human visual interpretation relying on Landsat satellite remote sensing images. The categorization scheme includes cropland, forests, grassland, water, ice, urban, and barren. Soil textures, expressed as sand, silt, and clay content within each grid cell, are compiled from the 1:1,000,000 soil type map and the second national soil survey. Water resource subregions are divided  
135 by the China Geological Survey, including Zhungaer Basin, Pearl River Basin, Yangtze River Basin, Southwestern River Basin, Tarim Basin, Songhua River Basin, Changthang Region, Inner Mongolian Plateau Region, Liaohe River Basin, Yellow River Basin, Huaihe River Basin, Hexi Corridor Region, Haihe River Basin, Southeastern River Basin, and Qaidam Basin. Water resource subregions are based on the principles of groundwater systems and water cycles and are focused on the inherent features of groundwater resources within distinct natural units.

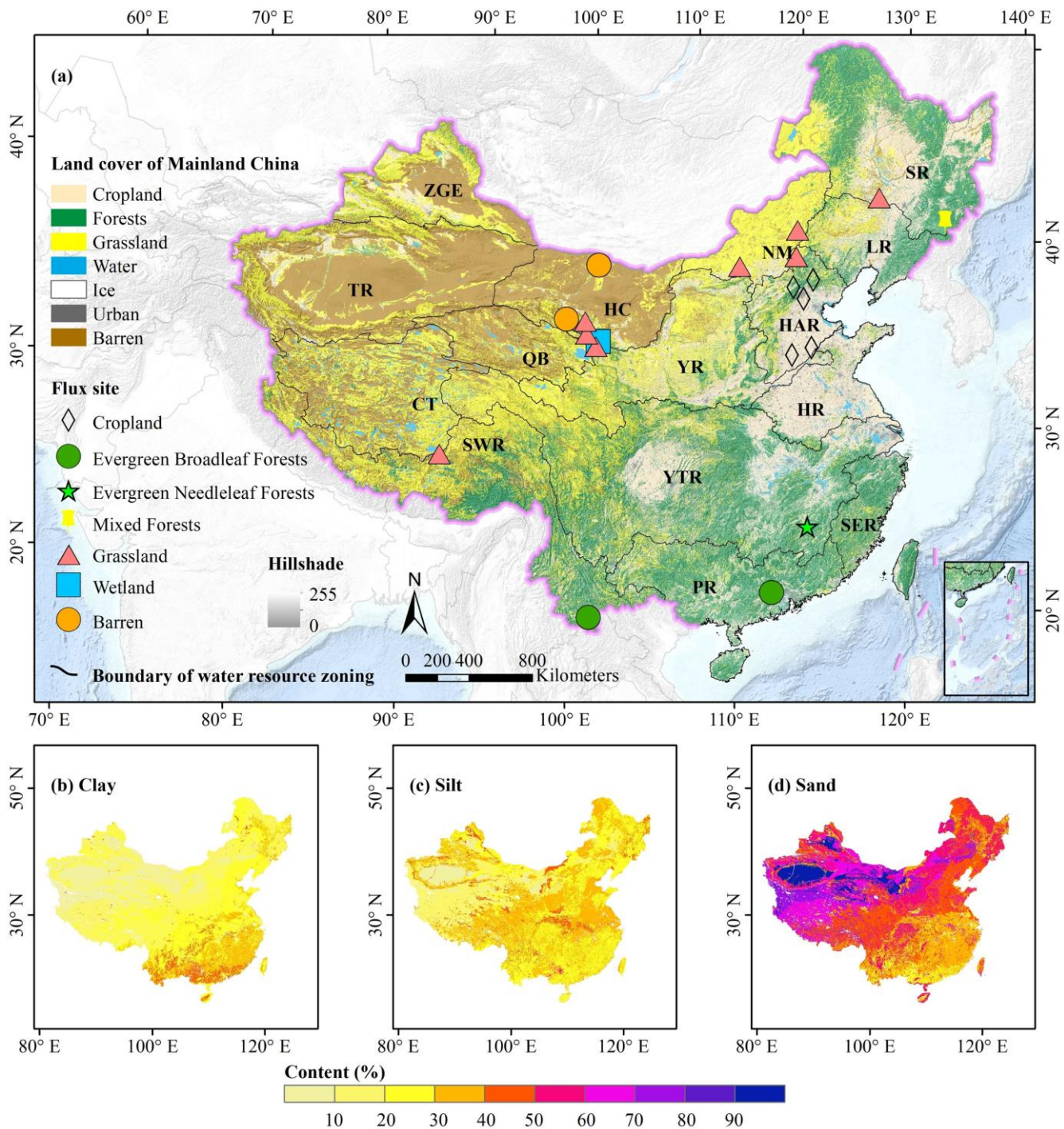


Figure 1: (a) Flux site locations, land cover types (2020), and water resource subregions of China. Distributions of (b) clay, (c) silt, and (d) sand content (1995). ZGE: Zhungar Basin, PR: Pearl River Basin, YTR: Yangtze River Basin, SWR: Southwestern River Basin, TR: Tarim Basin, SR: Songhua River Basin, CT: Changthang Region, NM: Inner Mongolian Plateau Region, LR: Liaohe

**Table 1: Flux site information used in this study.**

Site	Land cover types	Latitude	Longitude	Time span	Source
CN-Sw2		41.79	111.89	2011	Fluxnet
CN-Du2		42.04	116.28	2006–2008	Fluxnet
CN-Du3		42.05	116.28	2009–2010	Fluxnet
CN-Cng		44.59	123.51	2007–2010	Fluxnet
Damshung	Grassland	30.49	91.06	2004–2010	Chinaflux
Xilingela		43.53	116.67	2004–2010	Chinaflux
Haibei1		37.37	101.18	2003–2010	Chinaflux
Dashalong		38.84	98.94	2013–2015	TPDC
Arou		38.04	100.46	2013–2015	TPDC
Daxing		39.62	116.43	2008–2010	TPDC
Miyun		40.63	117.32	2008–2009	TPDC
Huailai	Cropland	40.35	115.79	2014–2018	TPDC
Guantao		36.52	115.13	2008–2009	TPDC
Yucheng		36.82	116.57	2003–2010	Chinaflux
Xishuangbanna	Evergreen broadleaf forests	21.92	101.26	2003–2010	Chinaflux
Dinghushan		23.16	112.53	2003–2010	Chinaflux
Qianyanzhou	Evergreen needleleaf forests	26.74	115.05	2003–2010	Chinaflux
Changbaishan	Mixed forests	42.40	128.09	2003–2010	Chinaflux
Haibei2	Wetland	37.66	101.33	2004–2009	Chinaflux
Huazhaizi	barren	38.76	100.32	2013–2015	TPDC
Luodi		41.99	101.13	2014–2015	TPDC

TPDC: National Tibetan Plateau Data Center

**Table 2: Spatial gridded data sets used in this study.**

Variable	Dataset	Spatial resolution	Temporal resolution	Unit	Time span	Reference
Soil moisture	SMCII.0	0.1°	day	0.001m <sup>3</sup> /m <sup>3</sup>	2000–2020	Li, Q. et al. (2022)
	GLASS	0.05°	8-day	W/m <sup>2</sup>	2000–2018	Yao et al. (2013, 2014)
Evapotranspiration	PML	500 m	day	0.01mm	2000–2020	Zhang et al. (2019) and He et al. (2022)
	CAMELE	0.1°	8-day	kg/ m <sup>2</sup> /s	2001–2019	Li, C. et al. (2022)
	SEBAL	1 km	day	mm	2001–2018	Cheng et al. (2021)
	GLASS	0.05°	8-day		1982–2018	Yuan et al. (2014)
Gross primary production	PML	500 m	day	gC/m <sup>2</sup>	2000–2020	Zhang et al. (2019) and He et al. (2022)
	GOSIF	0.05°	8-day		2000–2021	Li and Xiao (2019)
	TL	0.05°	8-day		1992–2020	Bi et al. (2022)
Specific humidity	-	0.1°	3-hour	kg kg <sup>-1</sup>	1979–2018	Yang et al. (2010) and

Air temperature				K		He et al. (2020)
Downward shortwave radiation				W m <sup>-2</sup>		
Precipitation				mm hr <sup>-1</sup>		
Land cover	-	1 km	-	-	2020	<a href="http://www.resdc.cn/">http://www.resdc.cn/</a>
Soil texture	-	1 km	-	-	1995	<a href="http://www.resdc.cn/">http://www.resdc.cn/</a>

## 2.2 Determination of CSM

150 CSM derived by the SM and EF method was used to assess the CSM using ET and GPP at the flux site. There must be both positive and negative metrics from the covariance and correlation-difference methods. For each grid cell and the entire period per year, negative metrics are displayed when SM is less than CSM, and positive metrics are shown when SM is greater than CSM. The data is taken into account just when the temperature surpasses 10° (Denissen et al., 2020) to avoid the influence of ice and snow, and the covariance between VPD and GPP must exhibit a minimum of 7 covariance values within  
155 9-day moving windows, with a minimum of 15 data (Fu et al., 2022b). Hence, we concentrated on the warm season, June–September, which includes 16 data each year with 8 covariance values within 9-value moving windows. CSM was conducted in each grid cell using satellite-based ET and GPP over the period 2001–2018.

### 2.2.1 Soil moisture-evaporative fraction method

Investigating the relationship between SM and EF in the dry period can isolate the transition from energy limitation to water  
160 limitation (Feldman et al., 2019). CSM captures the interconnectedness between SM and EF. If SM is greater than or less than CSM, the relationship between SM and EF appears as a flat line or a positive slope line. A linear-plus-plateau model characterizes the relationship precisely (Seneviratne et al., 2010; Schwingshackl et al., 2017):

$$EF = \begin{cases} EF_{\max} + S(SM - CSM), & \text{if } SM < CSM \\ EF_{\max}, & \text{if } SM \geq CSM \end{cases}, \quad (1)$$

where EF is the evaporative fraction defined as  $LE/(LE+H)$ ;  $EF_{\max}$  represents the maximum EF in the energy-limited stage,  
165 and S is the gradient in the water-limited stage. Here, specific estimated CSM was simultaneously estimated by the Monte Carlo method. For a set of optimal parameters, the Nash-Sutcliffe efficiency (Nash and Sutcliffe, 1970) above 0.5 was considered satisfactory (Herman et al., 2018). Thus, only 8 sites, including Xilingela in 2004, Damshung in 2004, CN-Sw2 in 2011, CN-Du2 in 2007, CN-Cng in 2010, Miyun in 2009, Huailai in 2015, and Qianyanzhou in 2010, were chosen for CSM detection. In addition, the Bayesian Information Criterion (BIC) (Schwarz, 1978) was used to select the best fit among  
170 three-segmented regression candidates (the flat line, the positive slope line, and the linear-plus-plateau). If the flat-line regression or the positive-slope regression outperformed the linear-plus-plateau regression, CSM was considered as not identified.



### 2.2.2 Covariance method

The covariance method presents a novel method for assessing ecosystem water stress in direct correlation with GPP, as illustrated by Fu et al. (2022b). It serves to quantify CSM over large areas. Positive covariances between VPD and GPP indicate that energy limits GPP. Negative covariances indicate that water limitation has a larger impact on GPP. VPD is determined by the disparity between the saturation vapor pressure ( $e_s$ ) and the actual vapor pressure ( $e_a$ ). Bolton (1980) posits that the calculation of  $e_a$  involves specific humidity (SH) and surface pressure (Pr):

$$e_a = \frac{SH \times Pr}{SH \times 0.378 + 0.622}, \quad (2)$$

### 180 2.2.3 Correlation-difference method

Another novel correlation-difference metric, proposed by Denissen et al. (2020), evaluates water versus energy-limited conditions using the detrended anomaly of VPD, ET, and SM:

$$\Delta_{\text{corr}} = \text{corr}(\text{ET}, \text{VPD}) - \text{corr}(\text{ET}, \text{SM}), \quad (3)$$

Matlab's corr tool calculates this metric, which uses Kendall's rank correlation (corr) rather than assuming linear correlations between variables (van Doorn et al., 2018). If  $\Delta_{\text{corr}} > 0$ , then the grid cell is in energy-limited regimes and vegetation anomalies (i.e., ET) correlate more strongly with energy anomalies (i.e., VPD) than with water anomalies (i.e., SM).  $\Delta_{\text{corr}} < 0$ , in contrast, the grid cell is in water-limited regimes. When  $\Delta_{\text{corr}} \approx 0$ , SM is labeled as CSM, indicating that water- and energy-limited regimes are transitioning.

## 2.3 Evaluation criteria

190 The correlation coefficient was applied to evaluate the performance of satellite-based ET from CAMELE, GLASS, PML, and SEBAL and GPP from GOSIF, GLASS, PML, and TL, compared to the eddy covariance observed in-situ ET and GPP. A point-to-pixel evaluation was carried out to evaluate the overestimation or underestimation of ET and GPP for each land cover type from all 21 flux sites. We summed 8-day ET and GPP in grassland, evergreen broadleaf forests, evergreen needleleaf forests, mixed forests, cropland, wetland, and barren land.

195 The alignment of CSM obtained by different methods was determined using the chi-square test (McHugh, 2013; Hsu and Dirmeyer, 2023a). CROSSTAB in MATLAB was used to perform the chi-square test. SM values were divided into two groups, below and above CSM. In this case, categorical data was tagged as a binary variable of 0 for drier than CSM and 1 for wetter than CSM. If there were significant differences with a 95% confidence level, CSM was different.

## 2.4 Partial least square regression

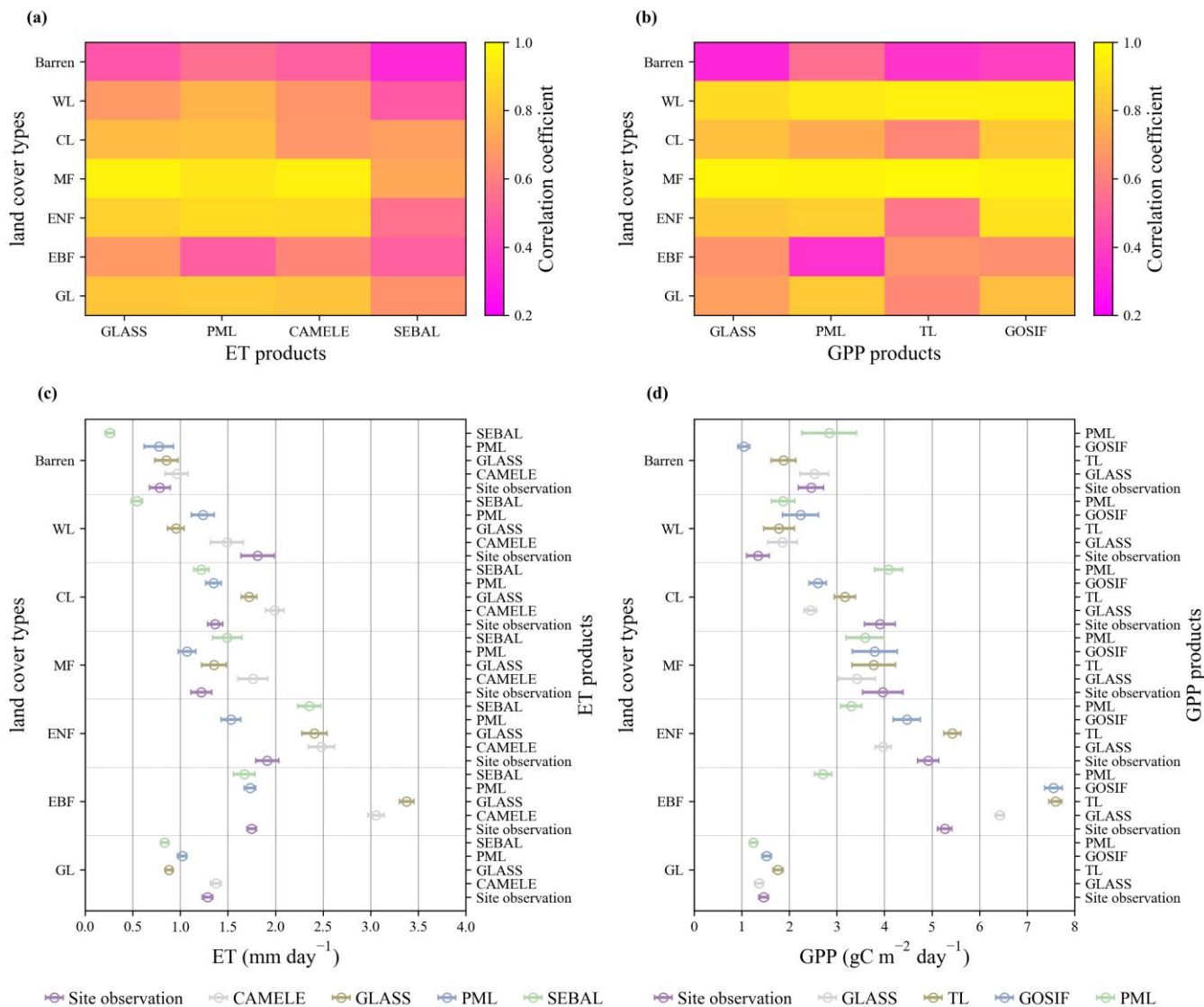
200 Partial least square regression has been widely acknowledged as a viable approach for mitigating collinearity issues among independent variables (Karthikeyan et al., 2020), which is extensively used in quantifying interannual impacts of climate and

plant growth variations on water and energy dynamics. Here, performances of the partial least square regression model were assessed by five-fold cross-validation using the mean absolute percentage error. The dominant factor (precipitation, temperature, incoming shortwave radiation, VPD, ET, GPP, or SM) of  $\Delta\text{corr}$  was identified by the largest variable importance in projection scores.

### 3 Results

#### 3.1 Consistency of ET and GPP

Figures 2a and b show good agreement between daily satellite-based products and site observations in most land cover types. Across all sites, correlation coefficients obtained from CAMELE, GLASS, PML, and SEBAL ET were 0.74, 0.65, 0.78, and 0.59, respectively; correlation coefficients obtained from GLASS, TL, GOSIF, and PML GPP were 0.75, 0.71, 0.77, and 0.74, respectively. For ET, the highest correlation coefficient occurred between GLASS and eddy covariance observations in mixed forests (0.96), while the lowest value was between SEBAL and site observations in barren (0.47). For GPP, the highest correlation coefficient was found between TL and site measurements in mixed forests (0.97), while the lowest value was between GLASS and site-based data in barren land (0.32). In general, no single product consistently outperformed others over all land cover types. As shown in Figures 2c and d, ET had the highest value in evergreen needleleaf forests and was the lowest in barren land, while GPP peaked in evergreen broadleaf forests and was the lowest in wetland. In these land cover types, ET and GPP derived from satellite-based products were also substantially different and varied quite a bit between different products. Especially in evergreen broadleaf forests, ET derived from GLASS (3.37 mm) and CAMELE (3.05 mm) and GPP from GOSIF ( $7.55 \text{ gC m}^{-2} \text{ day}^{-1}$ ) and TL ( $7.59 \text{ gC m}^{-2} \text{ day}^{-1}$ ) were higher than site observations of 1.74 mm and  $5.26 \text{ gC m}^{-2} \text{ day}^{-1}$ , respectively. If satellite-based ET and GPP were between  $\pm 10\%$  of site-observed values, they were termed as satisfactory; otherwise, they were either overestimated or underestimated. CAMELE, GLASS, PML, and SEBAL ET and GLASS, TL, GOSIF, and PML GPP met satisfied values in 1, 1, 3, 1, 2, 1, 3, and 2 land cover types, respectively. PML ET provided the most satisfactory estimates in evergreen broadleaf forests, cropland, and barren land with an average bias of 1.05%, 1.13%, and 1.34%, respectively; GOSIF GPP provided the most satisfactory estimate in grassland, evergreen needleleaf forests, and mixed forests with an average bias of 4.31%, 9.14%, and 4.29%, respectively. Although discrepancies existed among multi-source remotely sensed products across flux sites, they offered an opportunity to quantify characteristics of large-scale CSM and examine uncertainties from single-source data.



230 **Figure 2: Correlation coefficients between daily eddy covariance observations and satellite-based (a) ET and (b) GPP products and average (c) ET and (d) GPP across land cover types. The bars show 95% confidence intervals. GL: grassland, EBF: evergreen broadleaf forests, ENF: evergreen needleleaf forests, MF: mixed forests, WL: wetland.**

### 3.2 Consistency of CSM

Variations of SM and EF were depicted in Figure 3 for eight sites. Fitted lines represented controlling mechanisms in various evaporative regimes. Overall, the linear-plus-plateau regression with the lowest BIC outperformed the flat line and the  
 235 positive slope line in the study period. Specifically, CN-Du2 and Qianyanzhou sites showed a great slope at low SM values with BIC of -80.29 and -98.64, respectively. We also found that grassland CSM in different regions varied greatly. For example, grassland at Xilingela had the lowest CSM of 0.079 m<sup>3</sup>/m<sup>3</sup> with SM ranging from 0.06 to 0.20 m<sup>3</sup>/m<sup>3</sup>; CSM at

Damshung, Southwest China, was  $0.175 \text{ m}^3/\text{m}^3$  with SM ranging from 0.14 to  $0.26 \text{ m}^3/\text{m}^3$ ; CSM at CN-Cng in Northeast China was  $0.457 \text{ m}^3/\text{m}^3$  with high SM ranging from 0.30 to  $0.70 \text{ m}^3/\text{m}^3$ . Ranges of SM determined CSM value. Moreover, vertical lines of different colors represented CSM derived from  $\Delta\text{corr}$  using the correlation-difference method and covariance between VPD and GPP. To explore the performance of both methods on sites and whether they can be used on a large scale, the data applied to both methods was averaged for 8 days, consistent with gridded data. For CN-Du2 and Qianyanzhou sites, only positive or negative VPD-GPP covariance and  $\Delta\text{corr}$  were found. For Damshung, CN-Cng, and Huailai sites, we found more than one SM value where VPD-GPP covariance or  $\Delta\text{corr}$  was zero. Along with surface soil wetting, there was a change of VPD-GPP covariance and  $\Delta\text{corr}$  from positive to negative at these sites, inconsistent with the transition from water to energy limitation, indicating that CSM was not identifiable. Different from above, VPD-GPP covariance had the optimal CSM value that agreed best with the EF-SM-derived CSM at Xilingela and CN-Sw2 sites. Through another technique,  $\Delta\text{corr}$  was better than VPD-GPP covariance at Miyun site. In these sites, VPD-GPP covariance and  $\Delta\text{corr}$  changed from negative (water limit) to positive (energy limit). Therefore, VPD-GPP covariance and  $\Delta\text{corr}$  had the potential to obtain large-scale CSM.

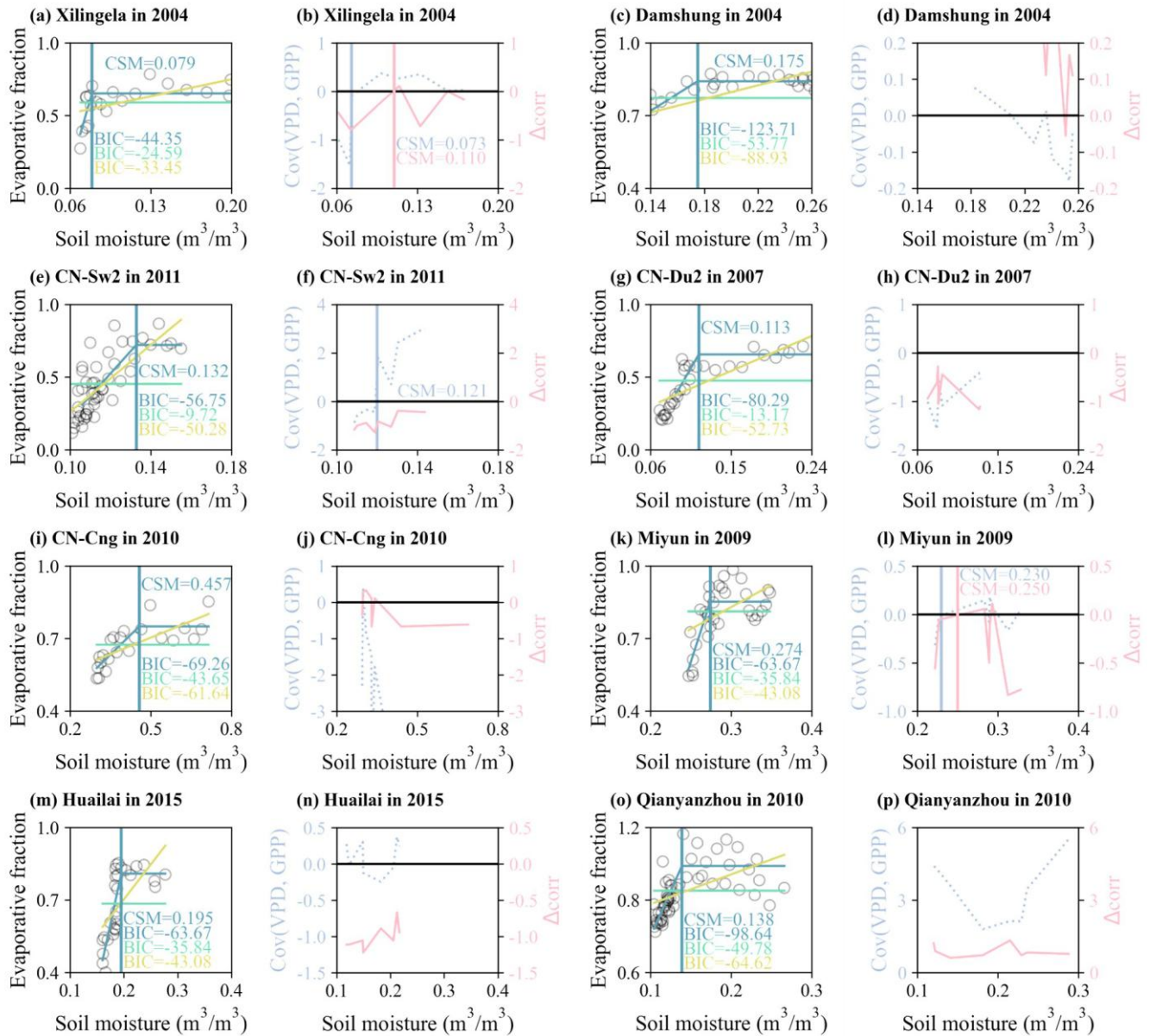


**Figure 3: Variations of soil moisture and evaporative fraction at (a) Xilingela in 2004, (c) Damshung in 2004, (e) CN-Sw2 in 2011, (g) CN-Du2 in 2007, (i) CN-Cng in 2010, (k) Miyun in 2009, (m) Huailai in 2015, (o) Qianyanzhou in 2010. Variations of covariance (referred to as Cov) between vapor pressure deficit (VPD) and gross primary production (GPP), and correlation-difference metric (referred to as  $\Delta_{corr}$ ) at (b) Xilingela in 2004, (d) Damshung in 2004, (f) CN-Sw2 in 2011, (h) CN-Du2 in 2007, (j) CN-Cng in 2010, (l) Miyun in 2009, (n) Huailai in 2015, (p) Qianyanzhou in 2010.**

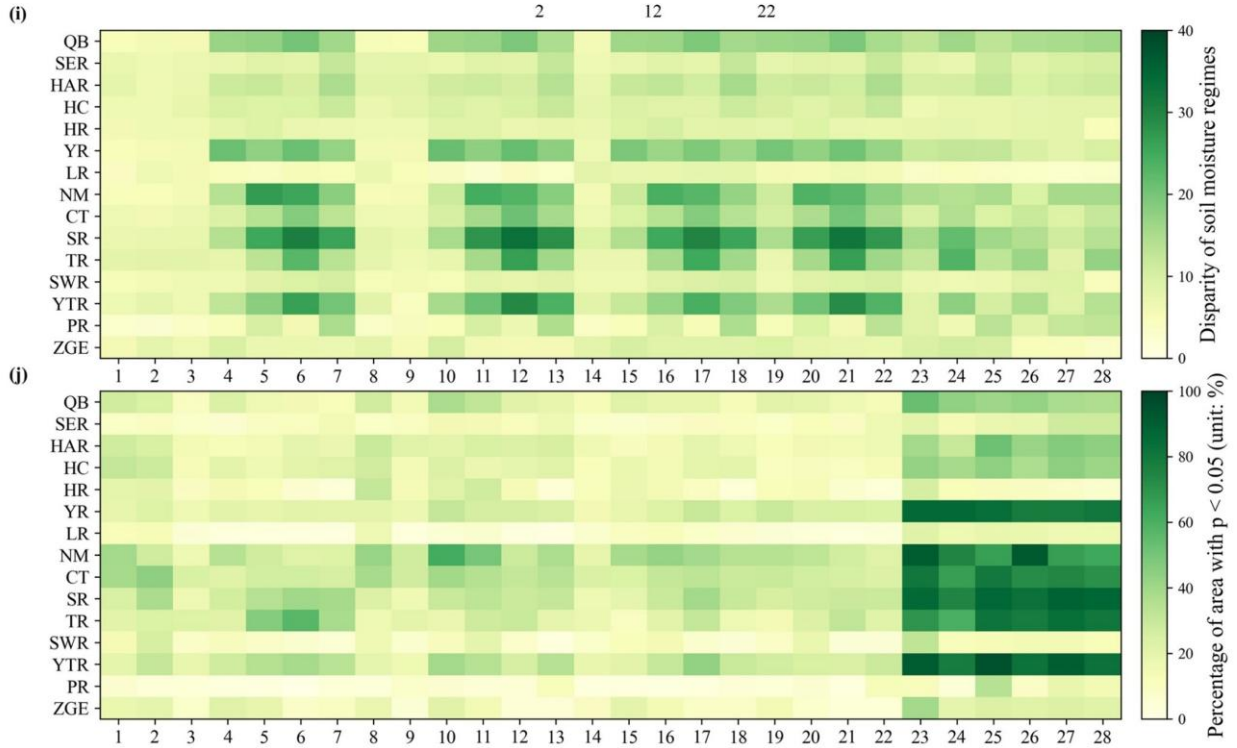
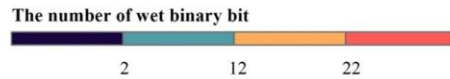
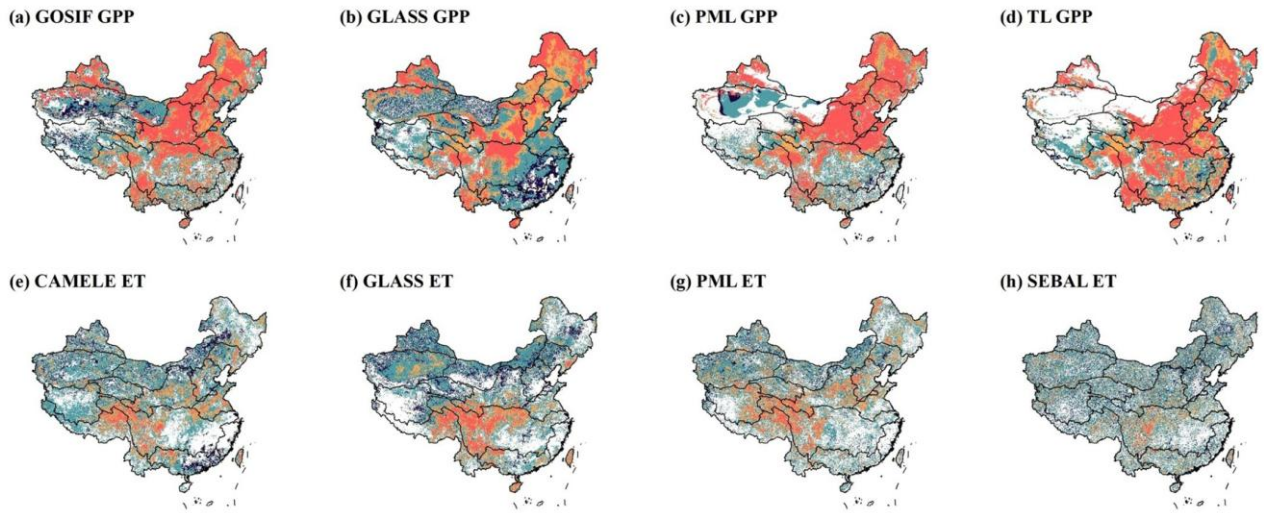
### 3.3 Spatial pattern of CSM

The number of wet binary bits was used to quantify the agreement among eight ET and GPP-based models at 10 cm soil depth. If CSM was identified, SM wetter than CSM was represented as 1, and 0 for others. If CSM was not identified within

260 a year, digits of the mode were treated as 0. If CSM was not detected for all 18 years, it was displayed as empty. The intercomparison provided helpful insights to examine consistency and discrepancy between multi-source ET and GPP products in depicting the spatial distribution of CSM. Figure 4 shows strong disparity in North and Central China, especially in Inner Mongolian Plateau Region, Songhua River Basin, Yangtze River Basin, and Yellow River Basin. In these regions, the chi-square test showed significant differences among GPP-based models due to their large number of wet binary bits. In addition, TL GPP displayed no CSM value in Northwest China. Note that the SM wetter-than-CSM showed agreement in eastern and southern basins, such as Huaihe River Basin, Liaohe River Basin, Southeastern River Basin, and Pearl River Basin, indicating that ET and GPP-based models were consistent in these basins.

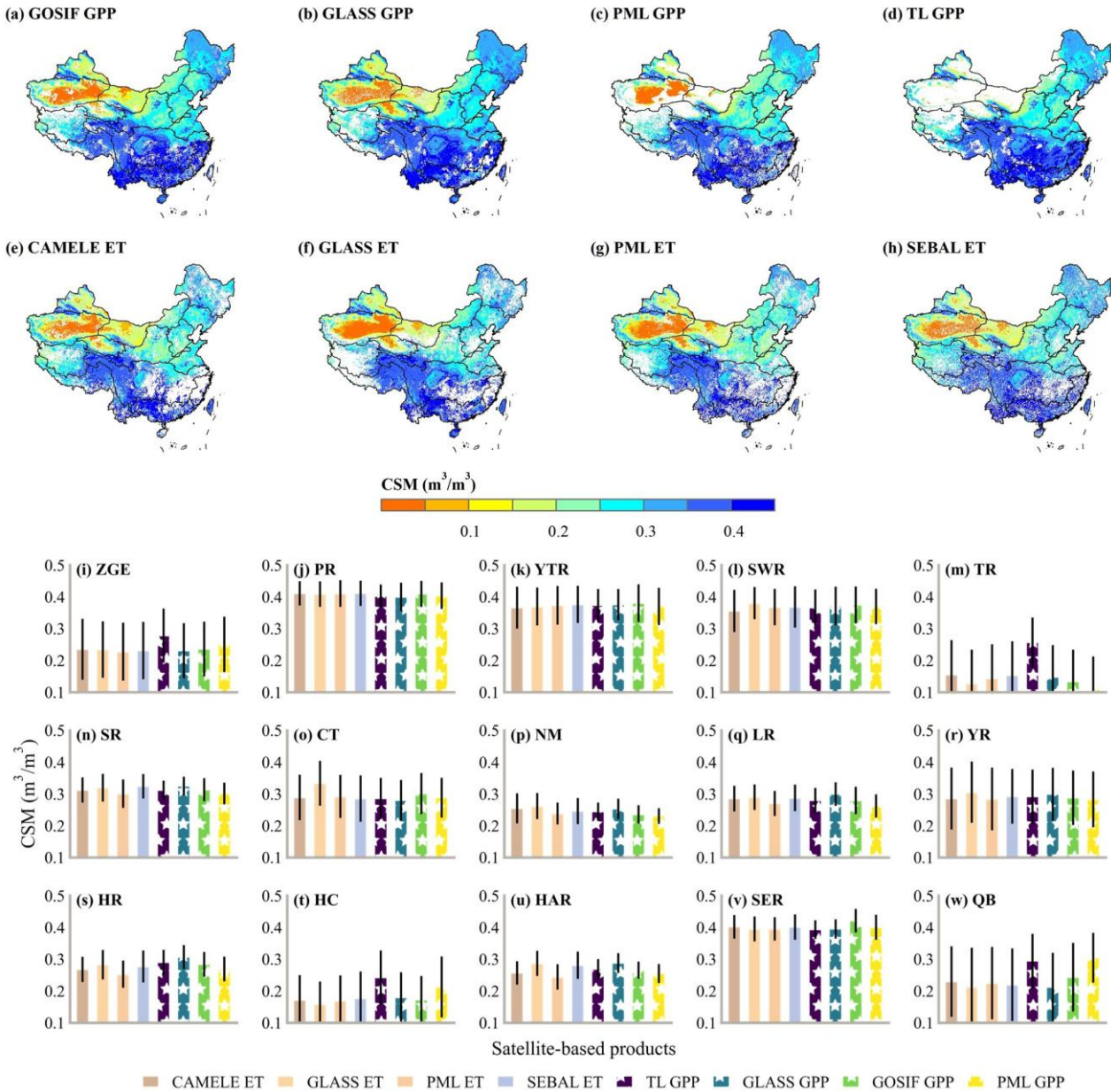
Figure 5 shows the spatial distribution of CSM obtained from covariance between VPD and GOSIF, GLASS, PML, and TL GPP, and correlation-difference metric with Kendall's rank correlation between the detrended anomaly of CAMELE, GLASS, PML, SEBAL ET and 10 cm soil depths SM and the correlation between the detrended anomaly of ET and VPD. Geographically, they spanned large swaths of land through water-scarce desert regions and lush, rainy forests. Overall, spatial patterns of CSM obtained through four ET products were consistent with those from four GPP products, showing a decreasing variation from south to north. Specifically for water resource subregions, CSM in semi-humid Huaihe River Basin, Haihe River Basin, and Yellow River Basin was about  $0.3 \text{ m}^3/\text{m}^3$ , respectively, and increased to approximately  $0.4 \text{ m}^3/\text{m}^3$  in Southeastern River Basin and Pearl River Basin. In addition, Table 3 shows the comparison of site-based CSM from EF-SM and grid-based CSM. It was found that gridded CSM values at CN-Cng, Miyun, and Huailai sites were generally consistent with site-based values. Gridded data had spatial continuity, while site observations showed significant differences in CSM even between adjacent sites (e.g., CN-Du2 of  $0.113 \text{ m}^3/\text{m}^3$  and Miyun of  $0.274 \text{ m}^3/\text{m}^3$ ), resulting in inconsistent CSM between satellite and site-based value.

280 Furthermore, large-scale CSM depended on roots pulling water out of the unsaturated soil matrix (Feldman et al., 2019) and varied across vegetation types and soil textures at four soil layers (Figure 6). With shorter root systems and less vegetation, barren areas showed low CSM. Forest regions displayed a relatively high CSM (e.g.,  $0.18 \text{ m}^3/\text{m}^3$  using PML ET and 10 cm depth SM). As for soil textures, sand covering the large area was further divided into content of less than 60%, 60–70%, 70–80%, 80–90%, and higher than 90%. Soil with a majority of clay had a wetter CSM than others (e.g.,  $0.38 \text{ m}^3/\text{m}^3$  using PML ET and 10 cm depth SM) and was to be expected given that clay had a larger negative matric potential compared to coarse soil textures dominated by sand and silt. In summary, fine soils and luxuriant vegetation had wetter CSM. Additionally, a layer-wise CSM analysis was conducted to highlight variations in SM properties for different soil layers. It was evident that there were variations in the CSM behavior across layers with higher SM and CSM at 20 cm soil depth. We also found that CSM for grassland and clay was higher than average SM at all four layers, which identified a large range of SM within water-limited regimes. However, for cropland and forests, differences existed in CSM among four ET-based methods, with higher CSM from GLASS and SEBAL than others.



- |                            |                            |                          |                            |                             |
|----------------------------|----------------------------|--------------------------|----------------------------|-----------------------------|
| 1: CAMELE ET and GLASS ET  | 8: GLASS ET and PML ET     | 14: PML ET and SEBAL ET  | 19: SEBAL ET and GLASS GPP | 23: GLASS GPP and GOSIF GPP |
| 2: CAMELE ET and PML ET    | 9: GLASS ET and SEBAL ET   | 15: PML ET and GLASS GPP | 20: SEBAL ET and GOSIF GPP | 24: GLASS GPP and PML GPP   |
| 3: CAMELE ET and SEBAL ET  | 10: GLASS ET and GLASS GPP | 16: PML ET and GOSIF GPP | 21: SEBAL ET and PML GPP   | 25: GLASS GPP and TL GPP    |
| 4: CAMELE ET and GLASS GPP | 11: GLASS ET and GOSIF GPP | 17: PML ET and PML GPP   | 22: SEBAL ET and TL GPP    | 26: GOSIF GPP and PML GPP   |
| 5: CAMELE ET and GOSIF GPP | 12: GLASS ET and PML GPP   | 18: PML ET and TL GPP    |                            | 27: GOSIF GPP and TL GPP    |
| 6: CAMELE ET and PML GPP   | 13: GLASS ET and TL GPP    |                          |                            | 28: PML GPP and TL GPP      |
| 7: CAMELE ET and TL GPP    |                            |                          |                            |                             |

295 Figure 4: Spatial pattern of wet binary bit number at 10 cm depth using covariance between vapor pressure deficit (VPD) and  
 300 gross primary production (GPP) from (a) GOSIF, (b) GLASS, (c) PML, (d) TL. Spatial pattern of wet binary bit number at 10 cm  
 depth using correlation-difference metric with Kendall's rank correlation between the detrended anomaly of soil moisture (SM)  
 and evapotranspiration (ET) from (e) CAMELE, (f) GLASS, (g) PML, and (h) SEBAL and the correlation between the detrended  
 anomaly of VPD and those ET products. (i) Disparity of soil moisture regimes among all methods and (j) percentage of area with  $p < 0.05$ .  
 ZGE: Zhungaer Basin, PR: Pearl River Basin, YTR: Yangtze River Basin, SWR: Southwestern River Basin, TR: Tarim Basin, SR: Songhua River Basin, CT: Changthang Region, NM: Inner Mongolian Plateau Region, LR: Liaohe River Basin, YR: Yellow River Basin, HR: Huaihe River Basin, HC: Hexi Corridor Region, HAR: Haihe River Basin, SER: Southeastern River Basin, QB: Qaidam Basin.



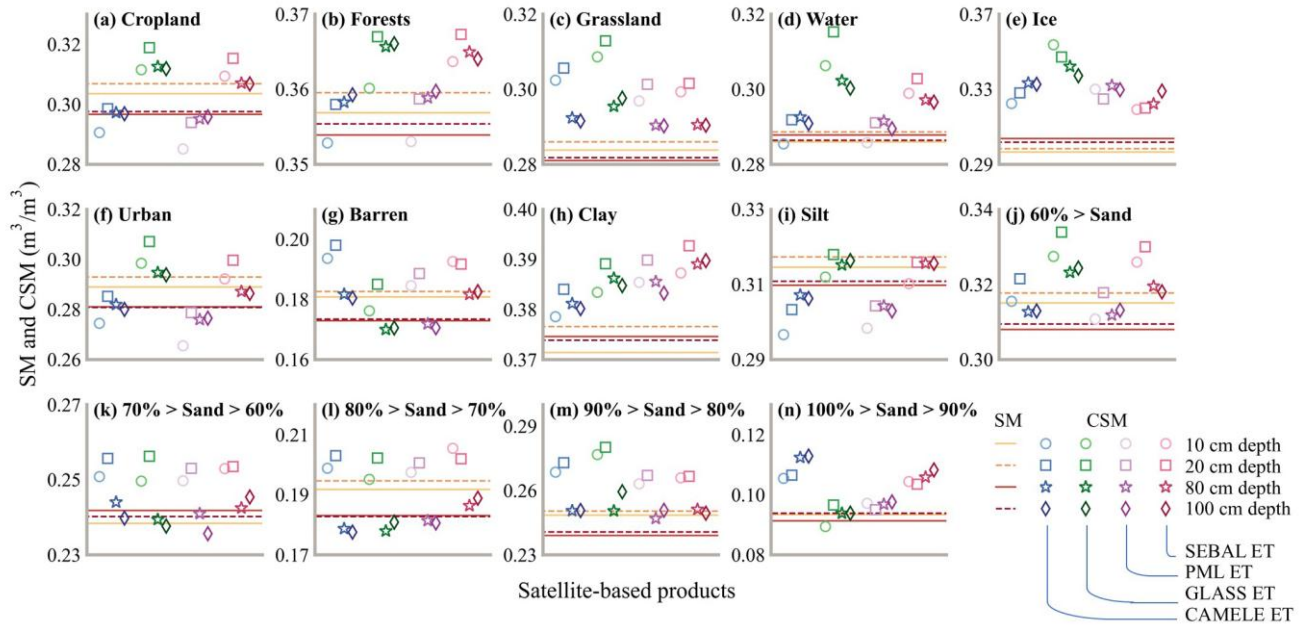


305 **Figure 5: Spatial pattern of critical soil moisture (CSM) at 10 cm depth using covariance between vapor pressure deficit (VPD) and gross primary production (GPP) from (a) GOSIF, (b) GLASS, (c) PML, (d) TL and CSM using correlation-difference metric with Kendall's rank correlation between the detrended anomaly soil moisture (SM) and evapotranspiration (ET) from (e) CAMELE, (f) GLASS, (g) PML, and (h) SEBAL and the correlation between the detrended anomaly VPD and those ET products. And (i–w) the basin-average values. ZGE: Zhungaer Basin, PR: Pearl River Basin, YTR: Yangtze River Basin, SWR: Southwestern River Basin, TR: Tarim Basin, SR: Songhua River Basin, CT: Changthang Region, NM: Inner Mongolian Plateau Region, LR: Liaohe River Basin, YR: Yellow River Basin, HR: Huaihe River Basin, HC: Hexi Corridor Region, HAR: Haihe River Basin, SER: Southeastern River Basin, QB: Qaidam Basin.**

310

**Table 3: Site-based CSM from EF-SM and grid-based CSM using satellite-based ET and GPP and 10 cm depth SM.**

Site	CSM from EF-SM	CSM using GOSIF GPP	CSM using GLASS GPP	CSM using PML GPP	CSM using TL GPP	CSM using CSMELE ET	CSM using GLASS ET	CSM using PML ET	CSM using SEBAL ET
Xilingela	0.079	0.249	0.263	0.250	0.251	0.266	0.303	-	0.296
Damshung	0.175	0.381	0.383	0.383	0.383	-	0.364	0.375	0.403
CN-Sw2	0.132	0.238	0.286	0.218	0.238	-	0.290	0.233	-
CN-Du2	0.113	0.275	0.300	0.252	0.277	0.260	0.299	-	0.292
CN-Cng	0.457	0.339	0.369	0.325	0.341	0.376	0.386	0.292	0.304
Miyun	0.274	0.315	0.336	0.294	0.331	0.304	0.322	0.311	0.316
Huailai	0.195	0.258	0.278	0.228	0.259	0.221	-	-	0.324
Qianyanzhou	0.138	0.452	0.407	0.327	0.418	-	-	-	-



315 **Figure 6: Soil moisture (SM) at 10 cm, 20 cm, 80 cm, and 100 cm soil depths, and critical soil moisture (CSM) derived from CAMELE, GLASS, PML, and SEBAL ET at corresponding soil depths for (a) cropland, (b) forests, (c) grassland, (d) water, (e) ice, (f) urban, (g) barren, soils with a majority of (h) clay, (i) silt, and sand with content (j) less than 60%, (k) between 60% and 70%, (l) between 70% and 80%, (m) between 80% and 90%, and (n) higher than 90%.**

### 3.4 Attribution of water and energy limit shifts

We assessed the spatial pattern of multi-annual average  $\Delta\text{corr}$  at 10 cm soil depth over the period 2001–2018. PML ET was used for  $\Delta\text{corr}$  given the fact that it had the best performance (Section 3.1). As shown in Figure 7a, water-limited regimes were most common in dry and semi-arid areas. Western and northern regions were generally water-limited, while southern regions were energy-limited. The cross-validation using partial least square regression shows that the variance that  $\Delta\text{corr}$  was explained by precipitation, temperature, incoming shortwave radiation, VPD, ET, GPP, and SM ranged from 73.34% in Yangtze River Basin to 99.95% in Haihe River Basin (Figure 7b).

Variations of dominant factors underlined the relevance of hydrological, meteorological, and ecological variables in inducing interannual changes in  $\Delta\text{corr}$ . As shown in Figure 8, blue pixels represented the significant decrease in  $\Delta\text{corr}$ , indicating increased water stress and correlation between ET and SM. Several typical regions had relatively large areas of significant decreases in  $\Delta\text{corr}$ , such as Changthang Region (2.62%) and Tarim Basin (3.49%). ET was the most important predictor across 42% of Changthang Region and 24% of Tarim Basin, which confirmed that increasing ET pushed increased water stress in these regions. In addition, a significant increase in VPD in the west might cause drought, especially in Tarim Basin, where VPD was the most important predictor across 19% of the area. For Haihe River Basin, decreasing SM contributed to increased water limitation. On the contrary, 4.29% of Hexi Corridor Region showed significant increases in  $\Delta\text{corr}$ ; increasing SM contributed to decreased water stress. 16.65% of Songhua River Basin showed significant increases in  $\Delta\text{corr}$ ; decreased water limitation was associated with increasing GPP (greening) in these regions. Moreover, ET and VPD played the most important role in 30% and 24% of Pearl River Basin, respectively; the significant decrease in VPD mitigated drought in these regions.

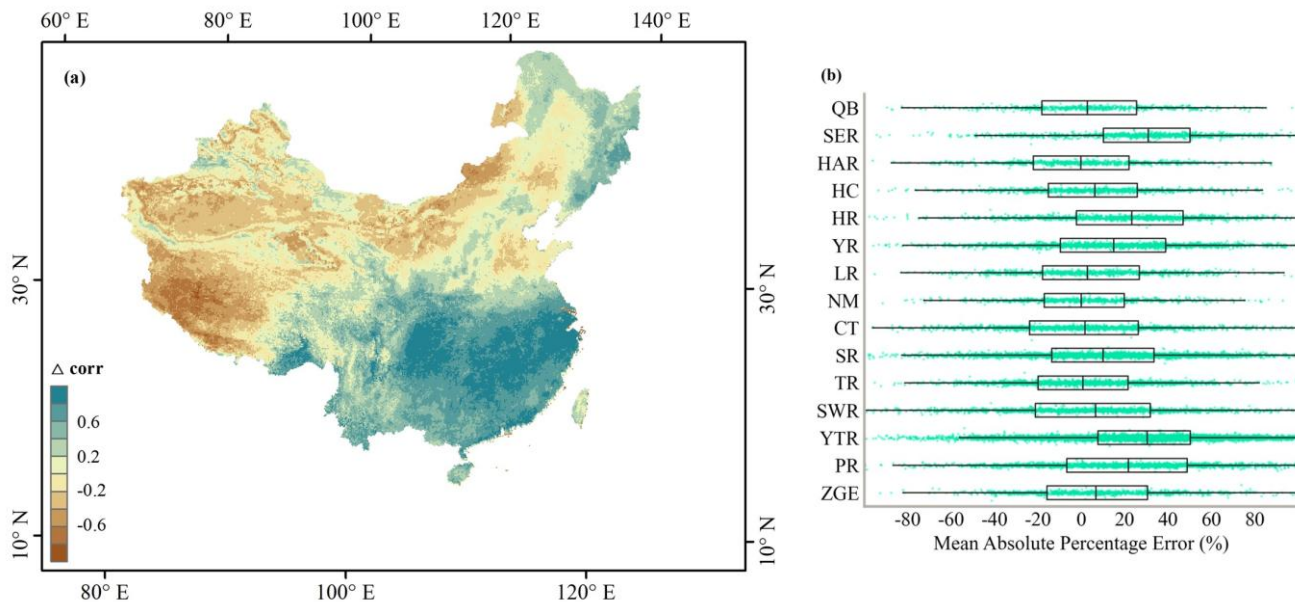
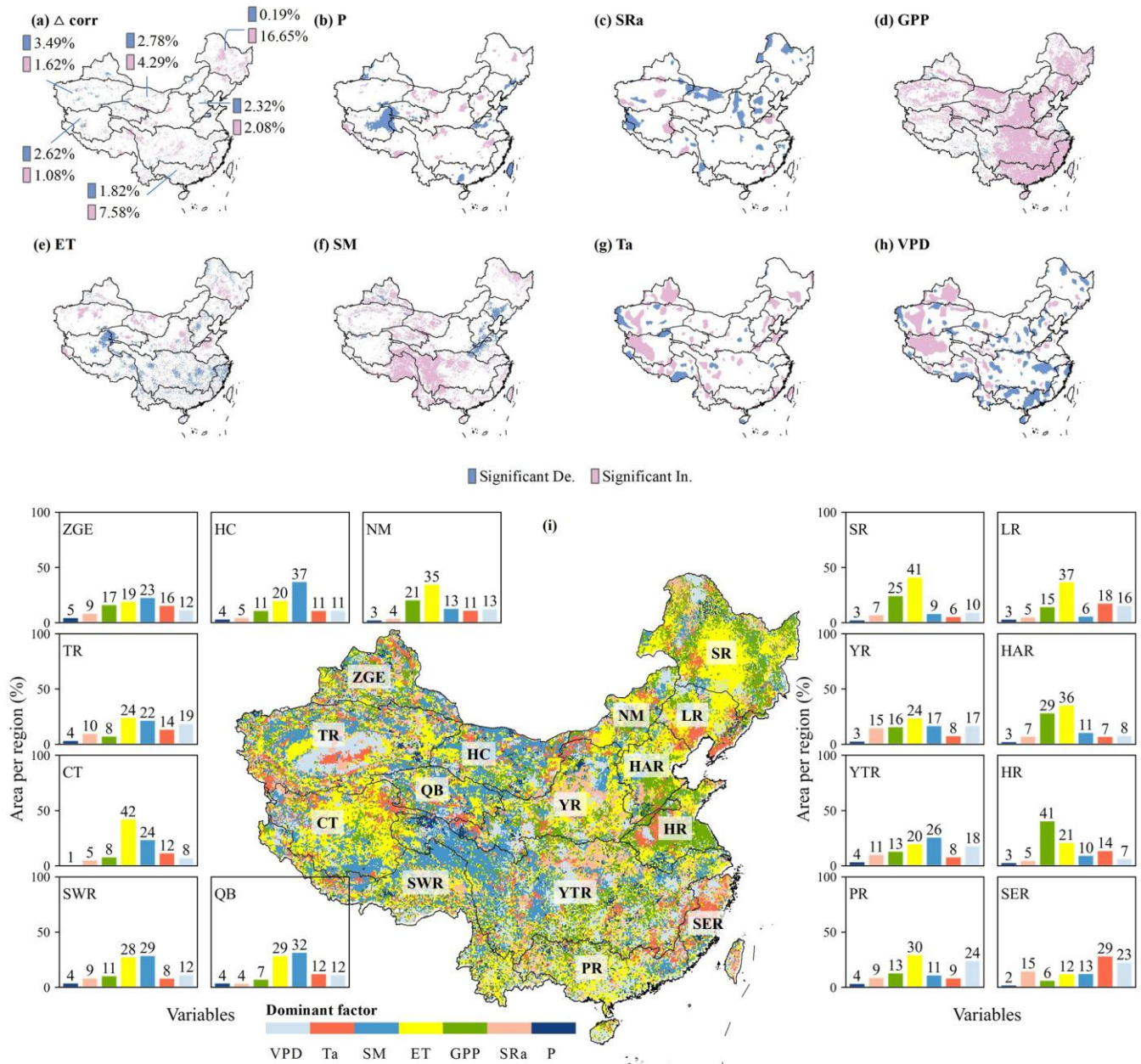


**Figure 7: Spatial pattern of (a)  $\Delta$ corr derived from PML ET and 10 cm soil depth soil moisture and (b) the mean absolute percentage error based on partial least square regression for  $\Delta$ corr estimations. ZGE: Zhungar Basin, PR: Pearl River Basin, YTR: Yangtze River Basin, SWR: Southwestern River Basin, TR: Tarim Basin, SR: Songhua River Basin, CT: Changthang Region, NM: Inner Mongolian Plateau Region, LR: Liaohe River Basin, YR: Yellow River Basin, HR: Huaihe River Basin, HC: Hexi Corridor Region, HAR: Haihe River Basin, SER: Southeastern River Basin, QB: Qaidam Basin.**



345 **Figure 8: Spatial pattern of significance ( $p < 0.05$ ) of (a)  $\Delta\text{corr}$ , (b) precipitation (P), (c) incoming shortwave radiation (SRa), (d) GOSIF gross primary production (GPP), (e) PML evapotranspiration (ET), (f) soil moisture (SM), (g) temperature (Ta), and (h) vapor pressure deficit (VPD) during the period of  $\Delta\text{corr}$  detection using the Mann–Kendall test (Mann, 1945; Kendall, 1948). “De.” means “decreasing” and “In.” means “increasing”. (i) Attribution of  $\Delta\text{corr}$  variations. Colors indicate the variable that best predicts  $\Delta\text{corr}$  dynamics. ZGE: Zhungaer Basin, PR: Pearl River Basin, YTR: Yangtze River Basin, SWR: Southwestern River Basin, TR: Tarim Basin, SR: Songhua River Basin, CT: Changthang Region, NM: Inner Mongolian Plateau Region, LR: Liaohe River Basin, YR: Yellow River Basin, HR: Huaihe River Basin, HC: Hexi Corridor Region, HAR: Haihe River Basin, SER: Southeastern River Basin, QB: Qaidam Basin.**

350

#### 4 Discussion

Analysis of spatial patterns of CSM using multi-source satellite-based water and carbon fluxes (Figure 2) derived from different methods (Figure 3) further enables us to effectively reflect variations from energy to water limitation in spatiotemporal continuous grid cells. To address the question of how soil textures and plant features define constraints imposed by water supply and energy availability, there has been a growing focus on CSM from site to continental scales. For instance, Northern California exhibits CSM of  $0.15 \text{ m}^3/\text{m}^3$  in semi-arid grassland at the site scale (Baldocchi et al., 2004); CSM using satellite-based surface temperature diurnal amplitude in semi-arid grassland of Africa has been reported to be  $0.12 \text{ m}^3/\text{m}^3$  at the continental scale (Feldman et al., 2019). For specific plants, CSM is around  $0.238 \text{ m}^3/\text{m}^3$  using PML ET in Inner Mongolian Plateau Region (Figure 5) where grass is abundant. That is in line with the grassland CSM of  $0.214 \text{ m}^3/\text{m}^3$  from the covariance approach across 195 global sites from the Integrated Carbon Observation System, the AmeriFlux, and the FLUXNET2015 (Fu et al., 2022a). Another study based on the correlation-difference method using SM from the European Space Agency Climate Change Initiative program and ET from the FLUXCOM reported large-scale CSM of around  $0.21 \text{ m}^3/\text{m}^3$  throughout Europe across all grid cells (Denissen et al., 2020). Researchers also found that plants exhibit a great vertical water uptake range to alleviate the impact of water stress (Gallego-Elvira et al., 2016), with water uptake extending to below 50 cm (Case et al., 2020) or 1–2 m (Tumber-Davila et al., 2022). Low CSM may be attributed to shorter rooting systems in water-limited environments (Konings and Gentine, 2017), while locations with high humidity, such as tropical West Africa and the southern part of Congo Basin (Feldman et al., 2022), exhibit high CSM. Deep-rooted forests can better regulate their response to drought with high CSM among soil layers, which means that root systems of plants play a key part in determining water- and energy-limited regimes and may help understand regional or continental-scale water- and energy-limited regimes that arise from different vegetation and soil conditions. To comprehend the underlying factors driving CSM, it is necessary to do a more comprehensive analysis of climate and ecosystem conditions: CSM detection shows that grassland had a large range of SM within water-limited regimes (Figure 6), where CSM was higher than average SM, probably because of shallow root systems affected by moisture; therefore, facing decreased  $\Delta\text{corr}$  (Figure 8), the grassland located in the northwestern arid region was more vulnerable. Further, water-limited regions exhibit great sensitivity in hydrologic cycles to variations in vegetation functioning, climate variability, and catchment physical conditions. Consequently, water-limited vegetation exhibits a higher degree of sensitivity to surface disturbances compared to locations with higher levels of precipitation. In this scenario, the effect of ET is more pronounced, resulting in a decline in energy

360

375

limitation, such as Tarim Basin. However, this study focusing on a specific time of year may not be enough to explain the critical value that may be shown in the rest of the year. Since CSM values in some grids are not detected by eight products, further research is needed for the CSM that may appear in the rest of the year in different regions. In addition, to compare the performance of multi-source remotely sensed water and carbon fluxes, all data is unified into the 8-day resolution. Therefore, a more refined time scale, such as a one-day scale study, is also needed.

Multiple factors contribute to inherent constraints in identifying different regimes associated with the utilization of multi-source satellite-based ET and GPP. For example, ET and GPP exhibit great uncertainties (Liu et al., 2021) in areas with barren land as indicated in Section 3.1. In eastern and southern regions, where satellite-based methods were more reliable, eight satellite-based SM regimes were in good agreement (Figure 4). Since the CAMELE ET combined PML ET, they showed consistency in cropland and forests with a lower CSM than GLASS and SEBAL (Section 3.3). By considering variations of energy and water limitations in terrestrial ecosystems (Section 3.4), there is potential to improve the water and carbon flux estimation in turn. In addition, SM from ground samplings and gridded sources (Koster et al., 2009) contributes to the uncertainty in characterizing CSM as discussed in Section 3.3. For gridded SM, surface climate shows a significant effect on the upper soil layer SM modeling, while the background aridity leads to low variability of the deeper layer SM (Li, Q. et al., 2022). Besides, external forcings seem to be responsible for a shift towards enhanced land-atmosphere coupling (Zhang et al., 2020). It should be noted that the South-to-North Water Diversion Project and the Pinglu Canal Project in China will result in significant modifications to SM characteristics, which are fundamental components of the concept known as CSM. Water management measures may reduce water stress in grasslands affected by climate change and make southern coastal clay areas more resistant to possible disturbances. Overall, our research can inform large-scale water conservancy projects for better water resource allocation from the perspective of the critical effect of SM.

## 5 Conclusion

Our main accomplishment is observing and identifying water and energy limit shifts using multi-source satellite-based water and carbon fluxes over China. These shifts show which areas are more likely to be affected by climate change. To do so, we first examined the consistency of ET and GPP derived from the site- and satellite-based grid observations and the consistency of CSM derived from the EF-SM, covariance, and correlation-difference methods. CSM detected by the covariance between VPD and GPP and CSM using the correlation-difference metric using VPD, ET, and SM matched well with CSM using the EF-SM method at the site scale, suggesting that these methods could detect large-scale CSM. According to satellite-based CSM from four ET products, four GPP products, and the latest SM dataset, surface water- and energy-limited regimes varied among land cover types, soil textures, and water resource subregions; soil textures of clay and land cover types of grassland had a large range of SM within water-limited regimes. Based on the spatial pattern of CSM, we further attributed the dominant factor of  $\Delta_{\text{corr}}$  and discovered that VPD was the most important predictor across 24% of Pearl River Basin and 19% of Tarim Basin. However, unlike the declining VPD in Pearl River Basin, the increasing VPD

410 aggravated the water stress in Tarim Basin, especially for the more fragile grassland in these areas. As environmental change and extreme disturbances affect CSM, future research directions will aim at the impact of hydraulic projects such as inter-basin water transfers on CSM, the impact of extreme disturbances such as tropical cyclones and wildfires on CSM, and possible changes in CSM.

This study used multi-source satellite-based water and carbon fluxes and different methods to detect CSM, and more efforts  
415 were put into the evaluation and validation of CSM. 18 years of datasets used for CSM were quite typical of the long-term climatology of continental wetness. Since CSM, an emerging property, is generated by multiple processes occurring on the land surface, in the atmosphere, and at the interface between them, uncertainties of ET and GPP from the algorithm, uncertainties of SM from ground sampling, and enhanced land-atmosphere coupling due to external forcing all contribute to CSM uncertainties. We emphasize that SM behavior below and above CSM determines ET and GPP and that water-limited  
420 regimes of the SM range depend on CSM. Water and carbon fluxes are vulnerable to the sensitivity of  $\Delta_{\text{corr}}$  to hydrological, meteorological, and ecological predictors. Accordingly, the water and carbon algorithm should consider water-energy limit shifts to improve the simulation accuracy. Thus, applying our new understanding of  $\Delta_{\text{corr}}$  and CSM under changing land-atmosphere conditions will provide a more complete perspective of the evolution of regional terrestrial ecosystems over extended periods.

#### 425 **Data availability**

National Tibetan Plateau Data Center (TPDC) offers eight flux sites, consisting of four locations inside the Hexi Corridor Region (Huazhaizi, Dashalong, Luodi, and Arou) and four cropland sites within the Haihe River Basin (Guantao, Huailai, Miyun, and Daxing) with half-hour records (<http://data.tpdc.ac.cn/>). ChinaFlux offers data from Damshung, Xilingela, Xishuangbanna, Dinghushan, Qianyanzhou, Changbaishan, Yucheng, Haibei1, and Haibei2 flux sites  
430 (<http://www.chinaflux.org/>). Fluxnet includes four grassland sites, CN-Sw2, CN-Du2, CN-Du3, and CN-Cng with daily records, which are available at <https://fluxnet.org/data/download-data/>. PML provides ET and GPP on the TPDC website. GLASS ET and GPP are provided by <http://glass.umd.edu/>. CAMELE ET is available at Zenodo: <https://zenodo.org/record/6283239/>. SEBAL ET is publicly accessible from the Zenodo repository at <https://zenodo.org/records/10803216> and <https://zenodo.org/records/10803553>. TL GPP is available at  
435 <https://doi.org/10.5061/dryad.dfn2z352k>. GOSIF GPP is obtained from <https://globalecology.unh.edu/>. Gridded soil moisture and meteorological data are available in TPDC. Land cover types and soil textures were contributed by the Data Center for Resources and Environmental Sciences, Chinese Academy of Sciences (<http://www.resdc.cn/>).

## Author contributions

Yi Liu: investigation, methodology, formal analysis, conceptualization, writing (original draft and review and editing);  
440 Jingfeng Xiao: supervision, writing (review and editing); Xing Li: writing (review and editing); Yue Li: writing (review and editing).

## Competing interests

The contact author has declared that none of the authors has any competing interests.

## Financial support

445 Y. Liu acknowledges support from Guangxi Natural Science Foundation under Grant No. 2024GXNSFBA010180.

## References

- Akbar, R., Gianotti, D. J. S., McColl, K. A., Haghighi, E., Salvucci, G. D., and Entekhabi, D.: Estimation of Landscape Soil Water Losses from Satellite Observations of Soil Moisture, *Journal of Hydrometeorology*, 19, 871–889. <https://doi.org/10.1175/JHM-D-17-0200.1>, 2018.
- 450 Baldocchi, D. D., Xu, L. K., and Kiang, N.: How plant functional-type, weather, seasonal drought, and soil physical properties alter water and energy fluxes of an oak-grass savanna and an annual grassland, *Agricultural and Forest Meteorology*, 123, 13–39, <https://doi.org/10.1016/j.agrformet.2003.11.006>, 2004.
- Bi, W., He, W., Zhou, Y., Ju, W., Liu, Y., Liu, Y., Zhang, X., Wei, X., and Cheng, N.: A global 0.05 degrees dataset for gross primary production of sunlit and shaded vegetation canopies from 1992 to 2020, *Scientific Data*, 9, 213  
455 <https://doi.org/10.1038/s41597-022-01309-2>, 2022.
- Bolton, D.: The computation of equivalent potential temperature, *Mon. Weather Rev.*, 108, 1046–1053, <https://doi.org/10.1175/2008MWR2593.1>, 1980.
- Case, M. F., Nippert, J. B., Holdo, R. M., and Staver, A. C.: Root-niche separation between savanna trees and grasses is greater on sandier soils, *Journal of Ecology*, 108, 2298–2308, <https://doi.org/10.1111/1365-2745.13475>, 2020.
- 460 Cheng, M., Jiao, X., Li, B., Yu, X., Shao, M., and Jin, X.: Long time series of daily evapotranspiration in China based on the SEBAL model and multisource images and validation, *Earth System Science Data*, 13, 3995–4017, <https://doi.org/10.5194/essd-13-3995-2021>, 2021.
- Denissen, J. M. C., Teuling, A. J., Reichstein, M., and Orth, R.: Critical Soil Moisture Derived from Satellite Observations Over Europe, *Journal of Geophysical Research-Atmospheres*, 125, e2019JD031672, <https://doi.org/10.1029/2019JD031672>,  
465 2020.

- Dong, J., Akbar, R., Feldman, A. F., Gianotti, D. S., and Entekhabi, D.: Land Surfaces at the Tipping-Point for Water and Energy Balance Coupling, *Water Resources Research*, 59, e2022WR032472, <https://doi.org/10.1029/2022wr032472>, 2023.
- Duan, S. Q., Findell, K. I., and Fueglistaler, S. A.: Coherent Mechanistic Patterns of Tropical Land Hydroclimate Changes, *Geophysical Research Letters*, 50, e2022GL102285, <https://doi.org/10.1029/2022gl102285>, 2023.
- 470 Feldman, A. F., Gianotti, D. J. S., Trigo, I. F., Salvucci, G. D., and Entekhabi, D.: Satellite-Based Assessment of Land Surface Energy Partitioning-Soil Moisture Relationships and Effects of Confounding Variables, *Water Resources Research*, 55, 10657–10677, <https://doi.org/10.1029/2019WR025874>, 2019.
- Feldman, A. F., Short Gianotti, D. J., Trigo, I. F., Salvucci, G. D., and Entekhabi, D.: Observed Landscape Responsiveness to Climate Forcing, *Water Resources Research*, 58, e2021WR030316, <https://doi.org/10.1029/2021WR030316>, 2022.
- 475 Fu, Z., Ciais, P., Wigneron, J. P., Gentine, P., Feldman, A. F., Makowski, D., Viovy, N., Kemanian, A. R., Goll, D. S., Stoy, P. C., Prentice, I. C., Yakir, D., Liu, L., Ma, H., Li, X., Huang, Y., Yu, K., Zhu, P., Li, X., Zhu, Z., Lian, J., and Smith, W. K.: Global critical soil moisture thresholds of plant water stress, *Nature communications*, 15, 4826–4826, <https://doi.org/10.1038/s41467-024-49244-7>, 2024.
- Fu, Z., Ciais, P., Feldman, A. F., Gentine, P., Makowski, D., Prentice, I. C., Stoy, P. C., Bastos, A., and Wigneron, J.-P.:  
480 Critical soil moisture thresholds of plant water stress in terrestrial ecosystems, *Science advances*, 8, eabq7827, <https://doi.org/10.1126/sciadv.abq7827>, 2022a.
- Fu, Z., Ciais, P., Makowski, D., Bastos, A., Stoy, P. C., Ibrom, A., Knohl, A., Migliavacca, M., Cuntz, M., Sigut, L., Peichl, M., Loustau, D., El-Madany, T. S., Buchmann, N., Gharun, M., Janssens, I., Markwitz, C., Gruenwald, T., Rebmann, C., Molder, M., Varlagin, A., Mammarella, I., Kolari, P., Bernhofer, C., Heliasz, M., Vincke, C., Pitacco, A., Cremonese, E.,  
485 Foltynova, L., and Wigneron, J.-P.: Uncovering the critical soil moisture thresholds of plant water stress for European ecosystems, *Global Change Biology*, 28, 2111–2123, <https://doi.org/10.1111/gcb.16050>, 2022b.
- Gallego-Elvira, B., Taylor, C. M., Harris, P. P., Ghent, D., Veal, K. L., and Folwell, S. S.: Global observational diagnosis of soil moisture control on the land surface energy balance, *Geophysical Research Letters*, 43, 2623–2631, <https://doi.org/10.1002/2016GL068178>, 2016.
- 490 Gentine, P., Green, J. K., Guerin, M., Humphrey, V., Seneviratne, S. I., Zhang, Y., and Zhou, S.: Coupling between the terrestrial carbon and water cycles-a review, *Environmental Research Letters*, 14, 083003, <https://doi.org/10.1088/1748-9326/ab22d6>, 2019.
- Good, S. P., Noone, D., and Bowen, G.: Hydrologic connectivity constrains partitioning of global terrestrial water fluxes, *Science*, 349, 175–177, <https://doi.org/10.1126/science.aaa5931>, 2015.
- 495 Grossiord, C., Buckley, T. N., Cernusak, L. A., Novick, K. A., Poulter, B., Siegwolf, R. T. W., Sperry, J. S., and McDowell, N. G.: Plant responses to rising vapor pressure deficit, *New Phytologist*, 226, 1550–1566, <https://doi.org/10.1111/nph.16485>, 2020.



- Haghighi, E., Gianotti, D. J. S., Akbar, R., Salvucci, G. D., and Entekhabi, D.: Soil and Atmospheric Controls on the Land Surface Energy Balance: A Generalized Framework for Distinguishing Moisture-Limited and Energy-Limited Evaporation Regimes, *Water Resources Research*, 54, 1831–1851, <https://doi.org/10.1002/2017WR021729>, 2018.
- He, J., Yang, K., Tang, W., Lu, H., Qin, J., Chen, Y., and Li, X.: The first high-resolution meteorological forcing dataset for land process studies over China, *Scientific Data*, 7, 25, <https://doi.org/10.1038/s41597-020-0369-y>, 2020.
- He, S., Zhang, Y., Ma, N., Tian, J., Kong, D., and Liu, C.: A daily and 500 m coupled evapotranspiration and gross primary production product across China during 2000-2020, *Earth System Science Data*, 14, 5463–5488, <https://doi.org/10.5194/essd-14-5463-2022>, 2022.
- Herman, M. R., Nejadhashemi, A. P., Abouali, M., Hernandez-Suarez, J. S., Daneshvar, F., Zhang, Z., Anderson, M. C., Sadeghi, A. M., Hain, C. R., and Sharifi, A.: Evaluating the role of evapotranspiration remote sensing data in improving hydrological modeling predictability, *Journal of Hydrology*, 556, 39–49, <https://doi.org/10.1016/j.jhydrol.2017.11.009>, 2018.
- Homaei, A., Feddes, R. A., and Dirksen, C.: Simulation of root water uptake II. Non-uniform transient water stress using different reduction functions, *Agricultural Water Management*, 57, 111–126, [https://doi.org/10.1016/S0378-3774\(02\)00071-9](https://doi.org/10.1016/S0378-3774(02)00071-9), 2002.
- Hsu, H., and Dirmeyer, P. A.: Soil moisture-evaporation coupling shifts into new gears under increasing CO<sub>2</sub>, *Nature Communications*, 14, 1162, <https://doi.org/10.1038/s41467-023-36794-5>, 2023a.
- Hsu, H., and Dirmeyer, P. A.: Uncertainty in Projected Critical Soil Moisture Values in CMIP6 Affects the Interpretation of a More Moisture-Limited World, *Earths Future*, 11, e2023EF003511, <https://doi.org/10.1029/2023ef003511>, 2023b.
- Karthikeyan, L., Chawla, I., Mishra, A. K.: A review of remote sensing applications in agriculture for food security: Crop growth and yield, irrigation, and crop losses, *Journal of Hydrology*, 586: 124905, <https://doi.org/10.1016/j.jhydrol.2020.124905>, 2020.
- Kendall, M. G.: Rank Correlation Methods, Hafner 160 pp., <https://doi.org/10.1017/S0020268100013019>, 1948.
- Konings, A. G., and Gentile, P.: Global variations in ecosystem-scale isohyricity, *Global Change Biology*, 23, 891–905, <https://doi.org/10.1111/gcb.13389>. 2017.
- Koster, R. D., Guo, Z., Yang, R., Dirmeyer, P. A., Mitchell, K., and Puma, M. J.: On the Nature of Soil Moisture in Land Surface Models, *Journal of Climate*, 22, 4322–4335, <https://doi.org/10.1175/2009JCLI2832.1>, 2009.
- Laio, F., Porporato, A., Ridolfi, L., and Rodriguez-Iturbe, I.: Plants in water-controlled ecosystems: active role in hydrologic processes and response to water stress - II. Probabilistic soil moisture dynamics, *Advances in Water Resources*, 24, 707–723, [https://doi.org/10.1016/S0309-1708\(01\)00005-7](https://doi.org/10.1016/S0309-1708(01)00005-7), 2001.
- Li, C., Yang, H., Yang, W., Liu, Z., Jia, Y., Li, S., and Yang, D.: CAMELE: Collocation-Analyzed Multi-source Ensembled Land Evapotranspiration Data, *Earth Syst. Sci. Data Discuss*, [preprint], <https://doi.org/10.5194/essd-2021-456>, 2022.
- Li, F., Xiao, J., Chen, J., Ballantyne, A., Jin, K., Li, B., Abraha, M., and John, R.: Global water use efficiency saturation due to increased vapor pressure deficit, *Science*, 381, 672–677, <https://doi.org/10.1126/science.adf5041>, 2023.

- Li, Q., Shi, G., Shangguan, W., Nourani, V., Li, J., Li, L., Huang, F., Zhang, Y., Wang, C., Wang, D., Qiu, J., Lu, X., and Dai, Y.: A 1 km daily soil moisture dataset over China using in situ measurement and machine learning, *Earth System Science Data*, 14, 5267–5286, <https://doi.org/10.5194/essd-14-5267-2022>, 2022.
- Li, X., and Xiao, J.: Mapping Photosynthesis Solely from Solar-Induced Chlorophyll Fluorescence: A Global, Fine-  
535 Resolution Dataset of Gross Primary Production Derived from OCO-2, *Remote Sensing*, 11, 2563, <https://doi.org/10.3390/rs11212563>, 2019.
- Li, X., Ryu, Y., Xiao, J., Dechant, B., Liu, J., Li, B., Jeong, S., and Gentine, P.: New-generation geostationary satellite reveals widespread midday depression in dryland photosynthesis during 2020 western US heatwave, *Science Advances*, 9, eadi0775, <https://doi.org/10.1126/sciadv.adi0775>, 2023.
- 540 Liu, W., Mo, X., Liu, S., Lin, Z., and Lv, C.: Attributing the changes of grass growth, water consumed and water use efficiency over the Tibetan Plateau, *Journal of Hydrology*, 598, 126464, <https://doi.org/10.1016/j.jhydrol.2021.126464>, 2021.
- Liu, Y., Mo, X., Hu, S., Chen, X., and Liu, S.: Attribution analyses of evapotranspiration and gross primary productivity changes in Ziya-Daqing basins, China during 2001–2015, *Theoretical and Applied Climatology*, 139, 1175–1189, <https://doi.org/10.1007/s00704-019-03004-6>, 2020.
- 545 Liu, Y. Y., Dorigo, W. A., Parinussa, R. M., de Jeu, R. A. M., Wagner, W., McCabe, M. F., Evans, J. P., and van Dijk, A. I. J. M.: Trend-preserving blending of passive and active microwave soil moisture retrievals, *Remote Sensing of Environment*, 123, 280–297, <https://doi.org/10.1016/j.rse.2012.03.014>, 2012.
- Mann, H. B.: Non-parametric test against trend, *Econometrica*, 13, 245–259, <https://doi.org/10.2307/1907187>, 1945.
- McHugh, M. L.: The Chi-square test of independence, *Biochem. Med.*, 23, 143–149, <https://doi.org/10.11613/bm.2013.018>,  
550 2013.
- Nash, J.E., Sutcliffe, J.V.: River flow forecasting through conceptual models part I – a discussion of principles, *Journal of Hydrology*, 10, 282–290, [https://doi.org/10.1016/0022-1694\(70\)90255-6](https://doi.org/10.1016/0022-1694(70)90255-6), 1970.
- Porporato, A., D'Odorico, P., Laio, F., Ridolfi, L., and Rodriguez-Iturbe, I.: Ecohydrology of water-controlled ecosystems, *Advances in Water Resources*, 25, 1335–1348, [https://doi.org/10.1016/S0309-1708\(02\)00058-1](https://doi.org/10.1016/S0309-1708(02)00058-1), 2002.
- 555 Rodriguez-Iturbe, I.: Ecohydrology: A hydrologic perspective of climate-soil-vegetation dynamics, *Water Resources Research*, 36, 3–9, <https://doi.org/10.1029/1999WR900210>, 2000.
- Schwarz, G.: Estimating the Dimension of a Model. *The Annals of Statistics*, 6, 461–464, <https://doi.org/10.1214/aos/1176344136>, 1978.
- Schwingshackl, C., Hirschi, M., and Seneviratne, S. I.: Quantifying Spatiotemporal Variations of Soil Moisture Control on  
560 Surface Energy Balance and Near-Surface Air Temperature, *Journal of Climate*, 30, 7105–7124, <https://doi.org/10.1175/JCLI-D-16-0727.1>, 2017.
- Seneviratne, S. I., Corti, T., Davin, E. L., Hirschi, M., Jaeger, E. B., Lehner, I., Orlowsky, B., and Teuling, A. J.: Investigating soil moisture-climate interactions in a changing climate: A review, *Earth-Science Reviews*, 99, 125–161, <https://doi.org/10.1016/j.earscirev.2010.02.004>, 2010.

- 565 Seneviratne, S. I., Luethi, D., Litschi, M., and Schaer, C.: Land-atmosphere coupling and climate change in Europe, *Nature*, 443, 205–209, <https://doi.org/10.1038/nature05095>, 2006.
- Teuling, A. J., Uijlenhoet, R., van den Hurk, B., and Seneviratne, S. I.: Parameter Sensitivity in LSMs: An Analysis Using Stochastic Soil Moisture Models and ELDAS Soil Parameters, *Journal of Hydrometeorology*, 10, 751–765, <https://doi.org/10.1175/2008JHM1033.1>, 2009.
- 570 Tumber-Davila, S. J., Schenk, H. J., Du, E., and Jackson, R. B.: Plant sizes and shapes above and belowground and their interactions with climate, *New Phytologist*, 235, 1032–1056, <https://doi.org/10.1111/nph.18031>, 2022.
- van Doorn, J., Ly, A., Marsman, M., and Wagenmakers, E.-J.: Bayesian Inference for Kendall's Rank Correlation Coefficient, *American Statistician*, 72, 303–308, <https://doi.org/10.1080/00031305.2016.1264998>, 2018.
- Xiao, J.: Satellite evidence for significant biophysical consequences of the "Grain for Green" Program on the Loess Plateau in China, *Journal of Geophysical Research-Biogeosciences*, 119, 2261–2275, <https://doi.org/10.1002/2014JG002820>, 2014.
- 575 Yang, K., He, J., Tang, W., Qin, J., and Cheng, C. C. K.: On downward shortwave and longwave radiations over high altitude regions: Observation and modeling in the Tibetan Plateau, *Agricultural and Forest Meteorology*, 150, 38–46, <https://doi.org/10.1016/j.agrformet.2009.08.004>, 2010.
- Yao, Y., Liang, S., Cheng, J., Liu, S., Fisher, J. B., Zhang, X., Jia, K., Zhao, X., Qing, Q., Zhao, B., Han, S., Zhou, G., Zhou, G., Li, Y., and Zhao, S.: MODIS-driven estimation of terrestrial latent heat flux in China based on a modified Priestley-Taylor algorithm, *Agricultural and Forest Meteorology*, 171, 187–202, <https://doi.org/10.1016/j.agrformet.2012.11.016>, 2013.
- 580 Yao, Y., Liang, S., Li, X., Hong, Y., Fisher, J. B., Zhang, N., Chen, J., Cheng, J., Zhao, S., Zhang, X., Jiang, B., Sun, L., Jia, K., Wang, K., Chen, Y., Mu, Q., and Feng, F.: Bayesian multimodel estimation of global terrestrial latent heat flux from eddy covariance, meteorological, and satellite observations, *Journal of Geophysical Research-Atmospheres*, 119, 4521–4545, <https://doi.org/10.1002/2013JD020864>, 2014.
- Yuan, W., Cai, W., Xia, J., Chen, J., Liu, S., Dong, W., Merbold, L., Law, B., Arain, A., Beringer, J., Bernhofer, C., Black, A., Blanken, P. D., Cescatti, A., Chen, Y., Francois, L., Gianelle, D., Janssens, I. A., Jung, M., Kato, T., Kiely, G., Liu, D., Marcolla, B., Montagnani, L., Raschi, A., Rouspard, O., Varlagin, A., and Wohlfahrt, G.: Global comparison of light use efficiency models for simulating terrestrial vegetation gross primary production based on the La Thuile database, *Agricultural and Forest Meteorology*, 192, 108–120, <https://doi.org/10.1016/j.agrformet.2014.03.007>, 2014.
- 590 Yuan, W., Liu, S., Zhou, G., Zhou, G., Tieszen, L. L., Baldocchi, D., Bernhofer, C., Gholz, H., Goldstein, A. H., Goulden, M. L., Hollinger, D. Y., Hu, Y., Law, B. E., Stoy, P. C., Vesala, T., Wofsy, S. C., and AmeriFlux, C.: Deriving a light use efficiency model from eddy covariance flux data for predicting daily gross primary production across biomes, *Agricultural and Forest Meteorology*, 143, 189–207, <https://doi.org/10.1016/j.agrformet.2006.12.001>, 2007.
- Zhang, P., Jeong, J.-H., Yoon, J.-H., Kim, H., Wang, S. Y. S., Linderholm, H. W., Fang, K., Wu, X., and Chen, D.: Abrupt shift to hotter and drier climate over inner East Asia beyond the tipping point, *Science*, 370, 1095–+, <https://doi.org/10.1126/science.abb3368>, 2020.

Zhang, Y., Kong, D., Gan, R., Chiew, F. H. S., McVicar, T. R., Zhang, Q., and Yang, Y.: Coupled estimation of 500 m and  
600 8-day resolution global evapotranspiration and gross primary production in 2002–2017, *Remote Sensing of Environment*,  
222, 165–182, <https://doi.org/10.1016/j.rse.2018.12.031>, 2019.

Zhu, W., Wang, Y., and Jia, S.: A remote sensing-based method for daily evapotranspiration mapping and partitioning in a  
poorly gauged basin with arid ecosystems in the Qinghai-Tibet Plateau, *Journal of Hydrology*, 616, 128807,  
<https://doi.org/10.1016/j.jhydrol.2022.128807>, 2023.